Supplement of Atmos. Chem. Phys., 26, 15683–15719, 2026
https://doi.org/10.5194/acp-26-15683-2026-supplement
© Author(s) 2026. CC BY 4.0 License.



Atmospheric Chemistry and Physics
Open Access
EGU

*Supplement of*

# Tropospheric oxidation chemistry and methane growth: a process-based attribution of OH variability (2003–2022)

**Benjamin Gaubert et al.**

*Correspondence to:* Benjamin Gaubert (gaubert@ucar.edu) and Mohammad Amin Mirrezaei (amirrezaei@arizona.edu)

The copyright of individual parts of the supplement might differ from the article licence.

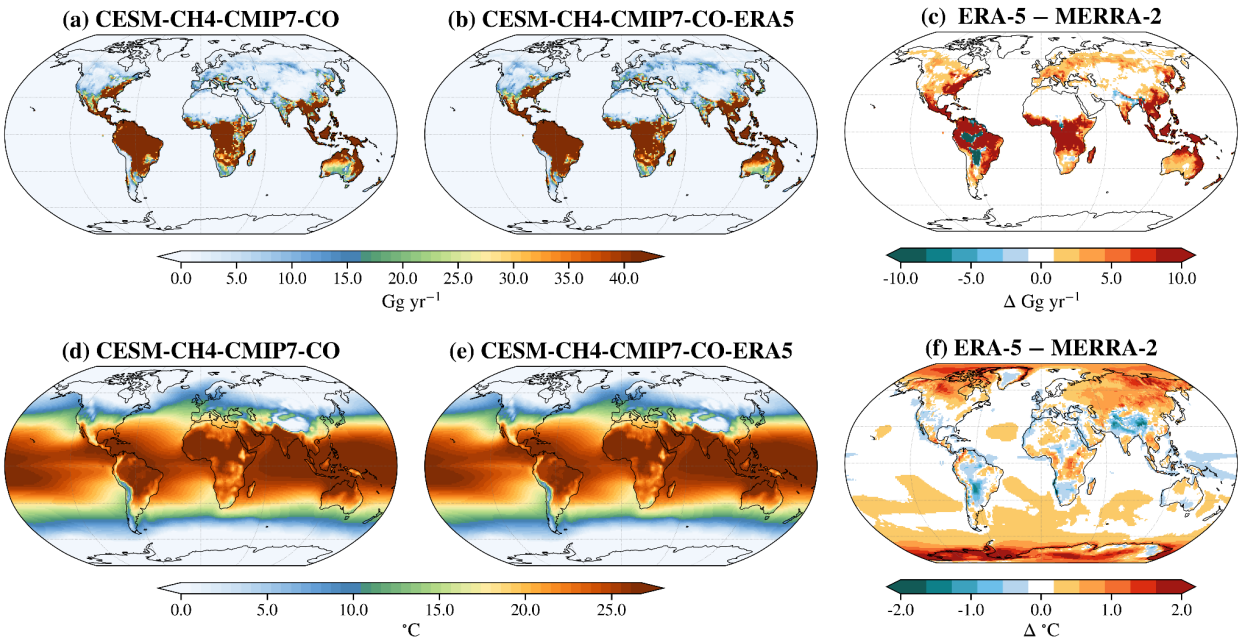



Figure S1. Annual-mean (2003–2022) maps of biogenic isoprene emission (top row) and surface temperature (bottom row) from two configurations that share identical emissions but differ in the meteorological reanalysis used for nudging: CESM-CH4-CMIP7-CO, driven by MERRA-2 (a, d), and CESM-CH4-CMIP7-CO-ERA5, driven by ERA-5 (b, e), together with their difference (ERA-5 − MERRA-2; c, f)

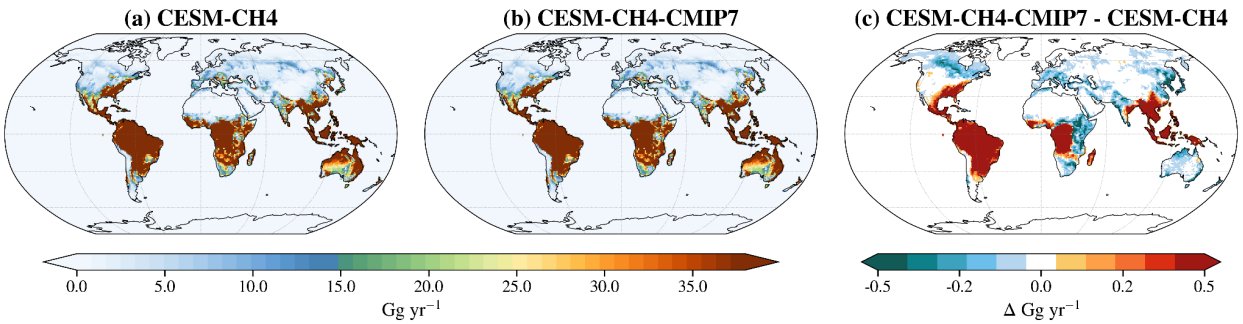



Figure S2. Annual-mean (2003–2022) biogenic isoprene emission (Gg $yr^{-1}$) for two configurations that share MERRA-2 meteorology but use different chemical-emission inventories: CESM-CH4 (CAMS + FINN, a) and CESM-CH4-CMIP7 (CMIP7/CEDS, b), together with their difference (CESM-CH4-CMIP7 − CESM-CH4; c).

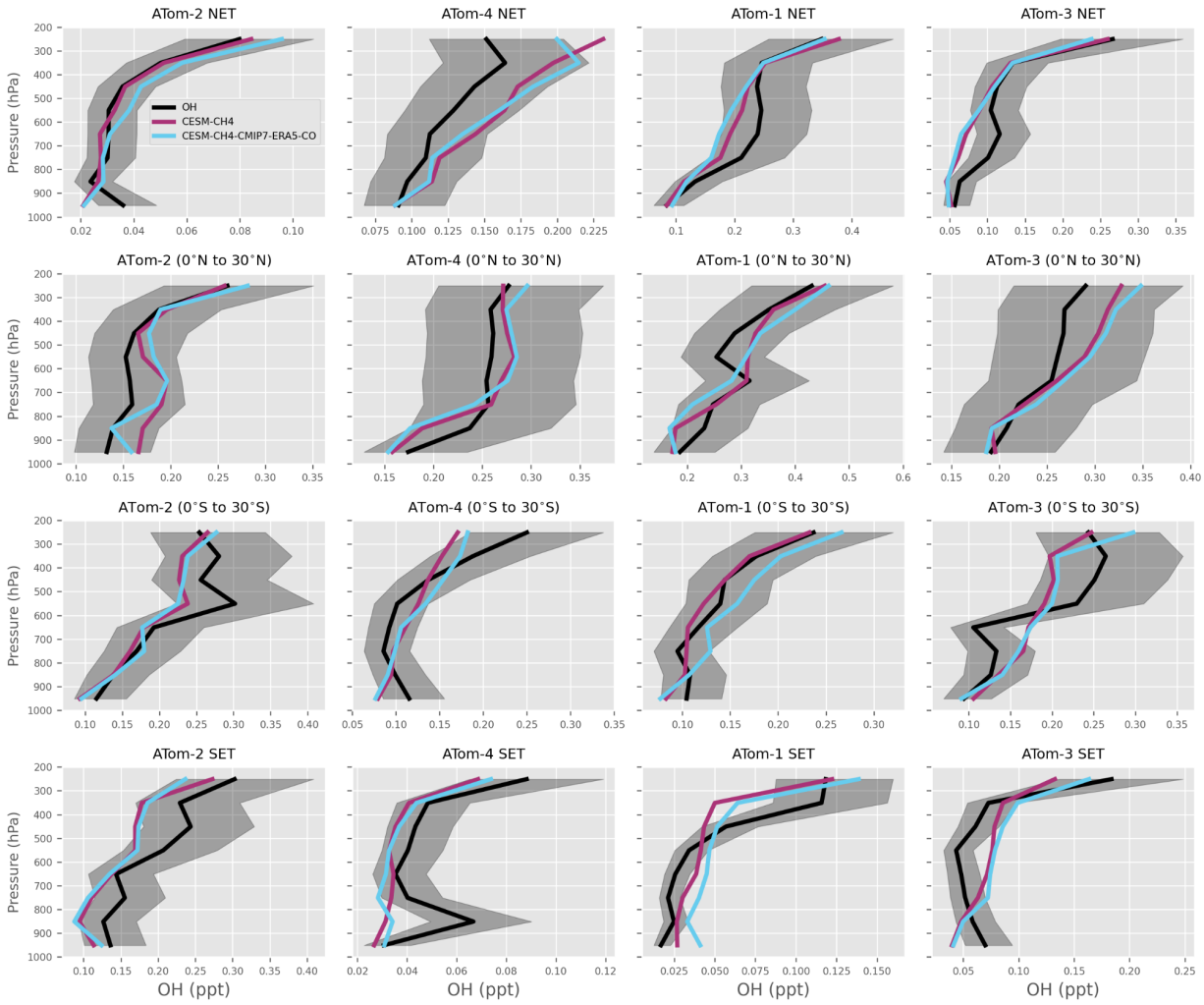



Figure S3. Evaluation of CESM-CH4 and CESM-CH4-CMIP7-CO-ERA5 OH simulations against NASA ATom measurements for 4 different latitudinal bands. The shaded areas indicate the measurement uncertainties and are estimated using a multiplicative uncertainty range of 1.35.

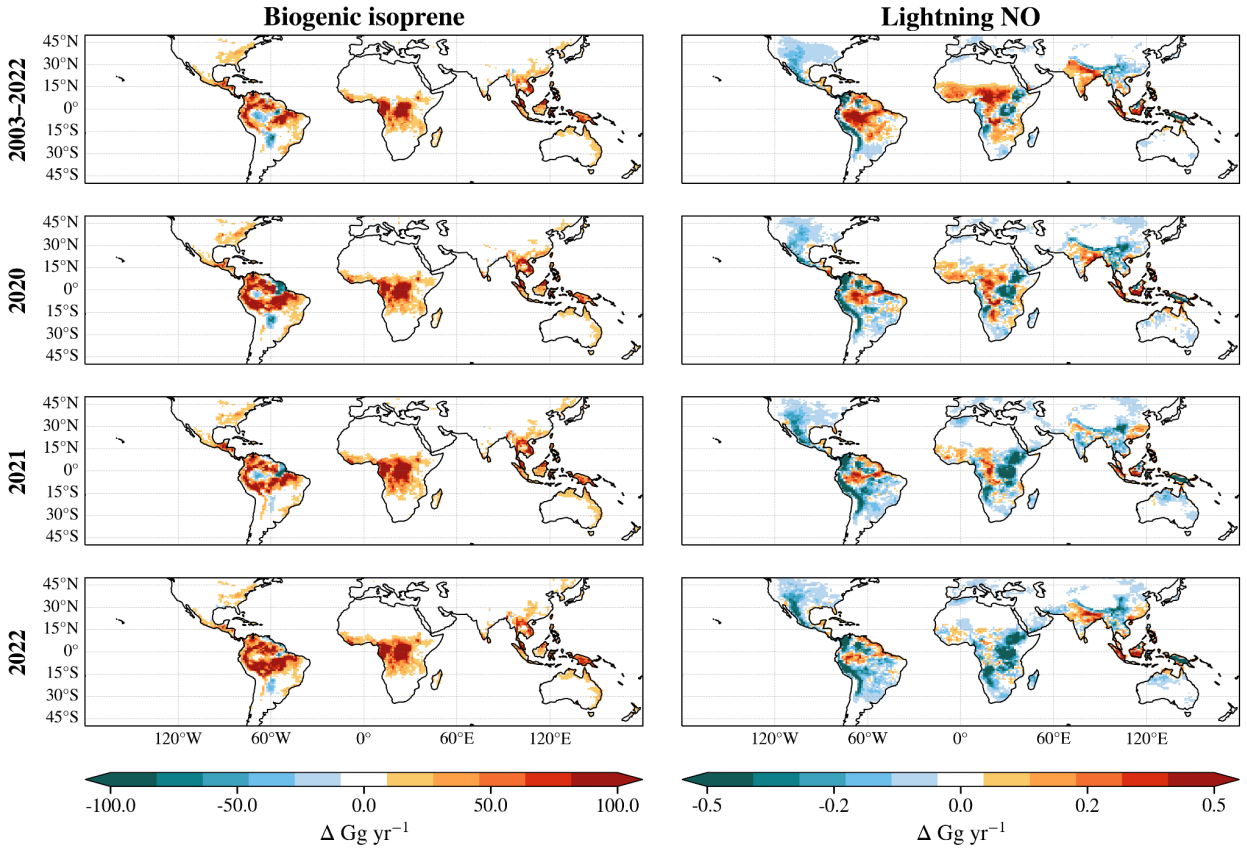



Figure S4. Differences in annual biogenic isoprene (left) and lightning NO (right) emission between the ERA5- and MERRA-2-driven runs (CESM-CH4-CMIP7-CO-ERA5 − CESM-CH4-CMIP7-CO).

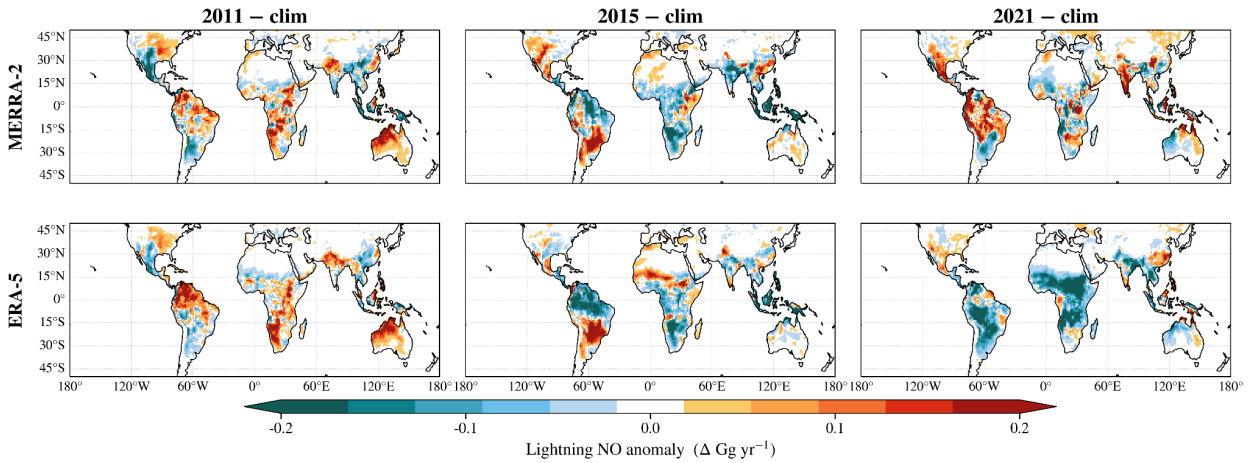



Figure S5. Lightning NO emission anomalies (individual year minus the 2003–2022 climatology) for three ENSO years, the La Niña years 2011 and 2021 and the strong El Niño year 2015, for the MERRA-2-driven simulation CESM-CH4-CMIP7-CO (top row) and the ERA-5-driven simulation CESM-CH4-CMIP7-CO-ERA5 (bottom row).

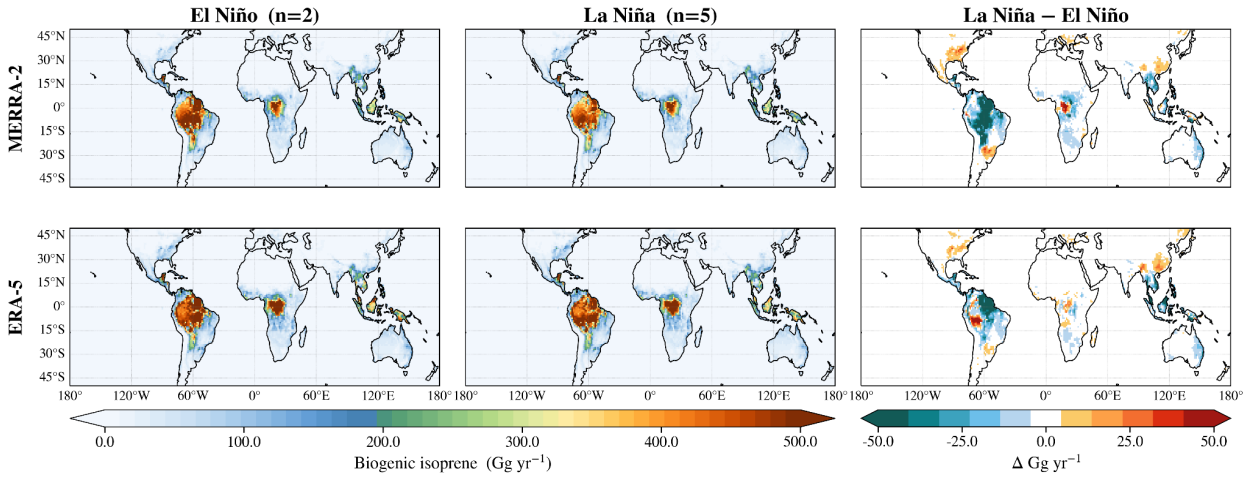



Figure S6. Biogenic isoprene emission (Gg $yr^{-1}$) averaged separately over El Niño years (2004 and 2015) and La Niña years (2007, 2008, 2011, 2021 and 2022), for the MERRA-2-driven simulation CESM-CH4-CMIP7-CO (top row) and the ERA-5-driven simulation CESM-CH4-CMIP7-CO-ERA5 (bottom row).

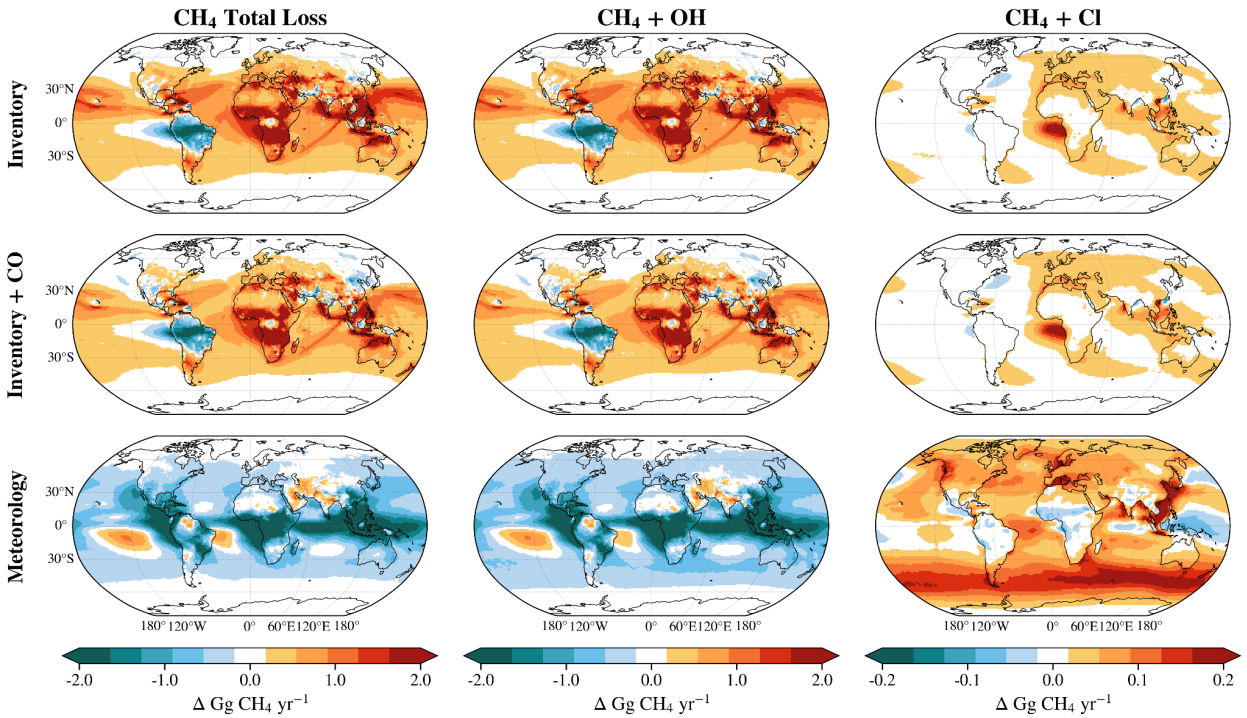



Figure S7. Climatological-mean (2003–2022) differences in $CH_4$ chemical loss between simulation pairs, isolating each driver: Inventory (CESM-CH4-CMIP7 − CESM-CH4), Inventory + CO (CESM-CH4-CMIP7-CO − CESM-CH4), and Meteorology (CESM-CH4-CMIP7-CO-ERA5 − CESM-CH4-CMIP7-CO). Columns show total $CH_4$ loss, $CH_4$ + OH and $CH_4$ + Cl.

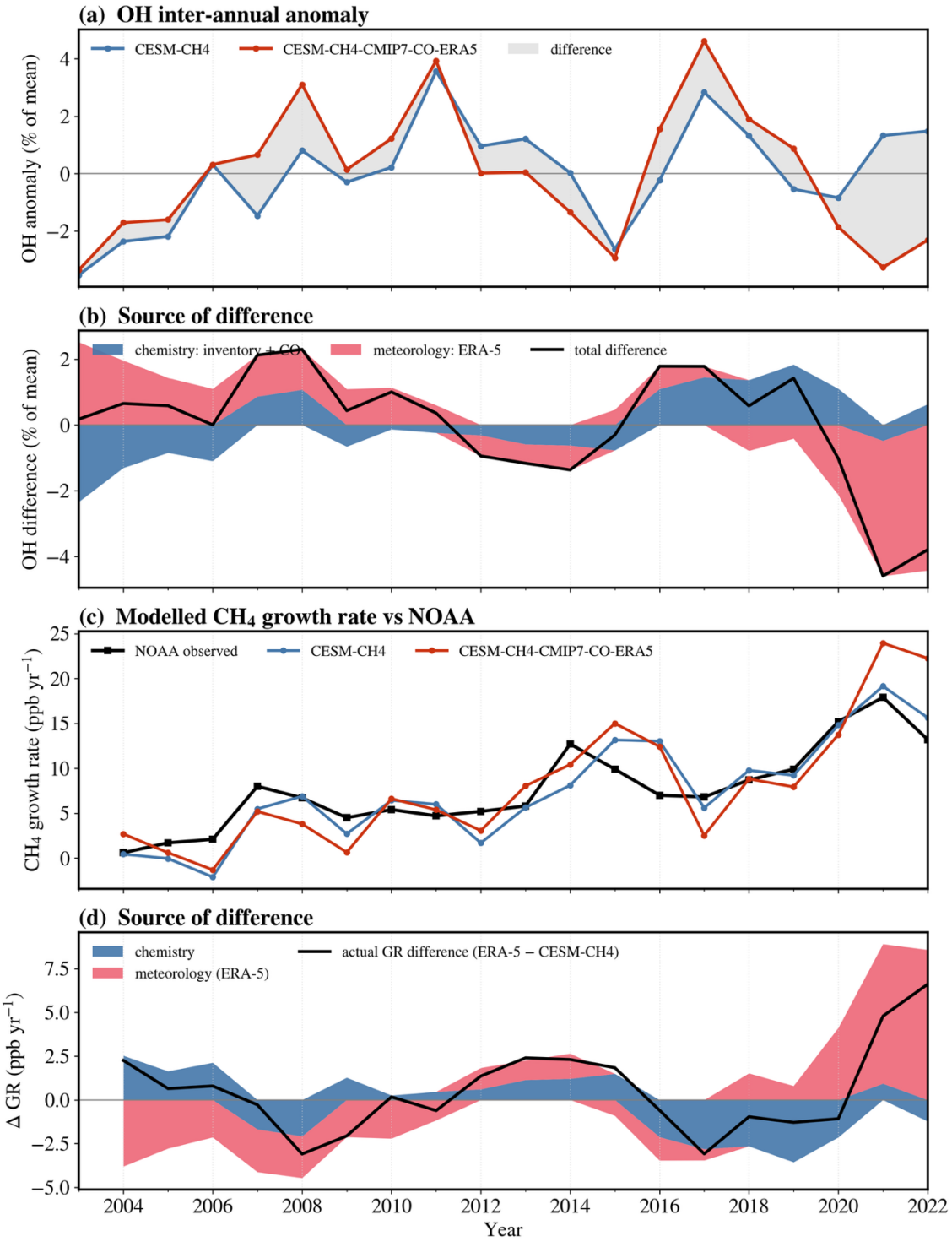



Figure S8. (a) OH inter-annual anomaly of the two best configurations and their difference; (b) the difference decomposes into chemistry (inventory + CO) and meteorology (ERA-5); (c) modelled $CH_4$ growth rate against NOAA; (d) the actual growth-rate spread against the contribution split into chemistry and meteorology.

## S1. Methane-loss-weighted OH

A methane-loss-weighted (air-mass-weighted) OH, following Lawrence et al. (2001), is considered in this study. The domain is divided into four zonal bands, northern extratropics (NET, 30–90°N), northern tropics (NT, 0–30°N), southern tropics (ST, 30°S–0), and southern extratropics (SET, 90–30°S), and each band (*r)* is given a weight equal to its share of the global $CH_4$+OH loss,

$$w_r = \frac{\bar{L_r}}{\sum_{r'} \bar{L_{r'}}},$$

where $\bar{L_r}$ is the time-mean tropospheric $CH_4$+OH loss in band r. The global loss-weighted OH anomaly is then

$$OH'(t) = \sum_r w_r \, OH'_r(t)$$

with $OH'_r$ the band-mean OH anomaly. We repeat the analysis with two alternatives, an air-mass weighting (using the well-mixed $CH_4$ burden as an air-mass proxy) and an OH-burden weighting, and find that the regional weights stay tropically dominated and the global driver ranking is essentially unchanged in both configurations

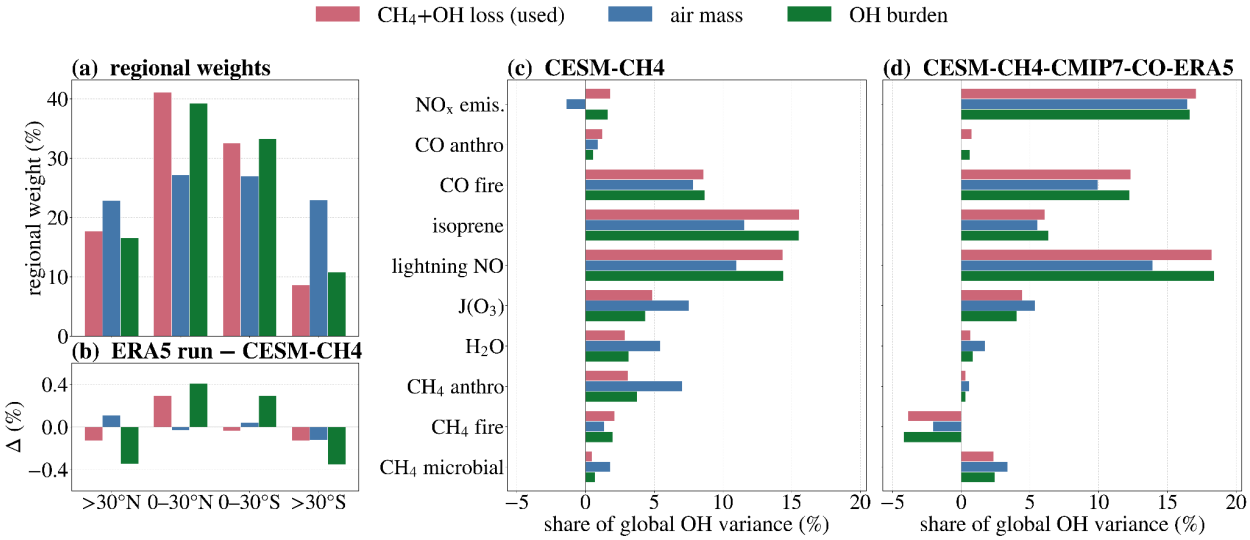



Figure S9. Weighting sensitivity of the attribution. (a) Regional weights $w_r$; for CESM-CH4 under the three weighting choices: $CH_4$ loss (used in this study), air mass and OH burden. (b) Difference in these weights between the two configurations (CESM-CH4-CMIP7-CO-ERA5 − CESM-CH4). (c, d) Resulting shares of the global OH variance for each forcing-basis driver in (c) CESM-CH4 and (d) CESM-CH4-CMIP7-CO-ERA5.

## S2. Regional regression and aggregation

Within each band, the OH anomaly is regressed on the local anomalies of a set of drivers by ordinary least squares,

$$OH'_r(t) = \sum_d \beta_{r,d}\, D'_{r,d}(t) + \varepsilon_r(t),$$

where $D'_{r,d}$ is the deseasonalized anomaly of driver $d$ in band $r$, $OH'_r$ the corresponding detrended OH anomaly, and $\beta_{r,d}$ its sensitivity. The per-band sensitivities are independent of the weighting; the weights enter only in aggregating the bands to the global scale. The global contribution of driver $d$ is the loss-weighted sum of its band-level contributions,

$$G_d(t) = \sum_r w_r\, \beta_{r,d}\, D'_{r,d}(t),$$

and the reconstruction of the global anomaly is the sum over drivers.

$$\widehat{OH'}(t) = \sum_d G_d(t)$$

and the share of driver $d$ is calculated from its covariance with the global anomaly rather than from its own variance,

$$S_d = 100 \frac{Cov[G_d(t), OH'(t)]}{Var[OH'(t)]},$$

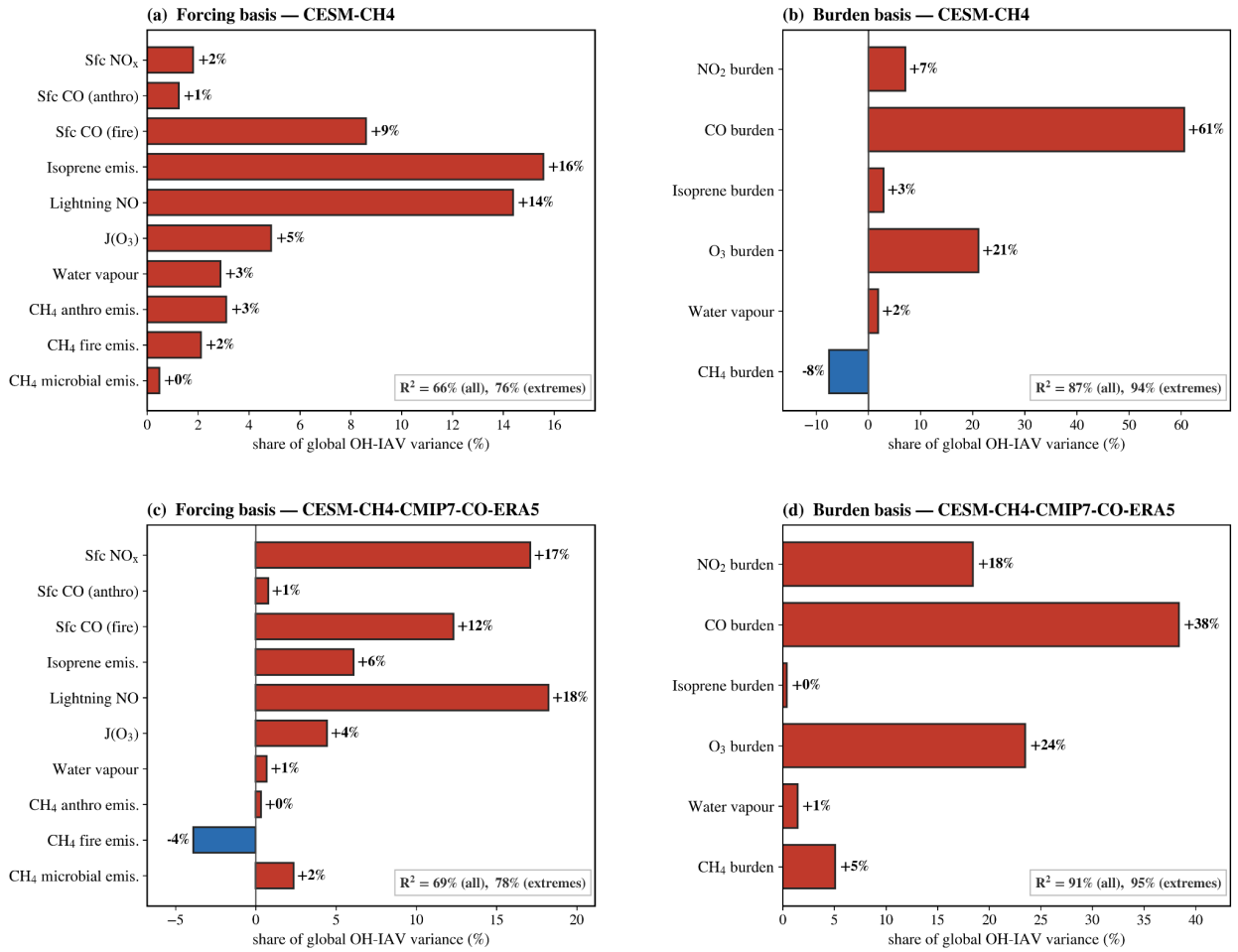



Figure S10. Driver attribution of the global OH-IAV variance for the two configurations (rows: CESM-CH4, top; CESM-CH4-CMIP7-CO-ERA5, bottom) in the forcing (left) and burden (right) bases, with reconstruction $R^2$.

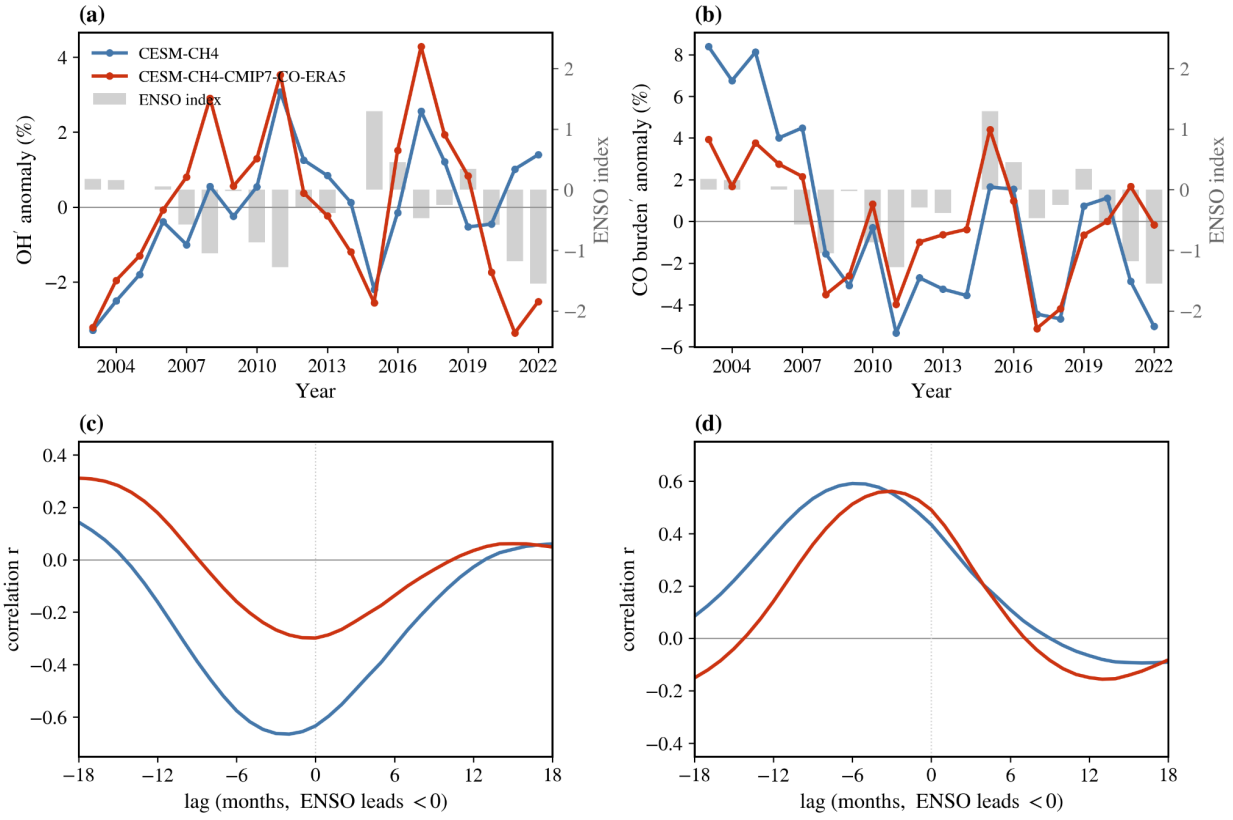



Figure S11. OH and CO-burden anomalies versus the ENSO index (MEI.v2), 2003–2022, for CESM-CH4 (blue) and CESM-CH4-CMIP7-CO-ERA5 (red). (a, b) Annual anomalies of (a) OH and (b) the CO burden (% of the 2003–2022 mean; left axes) with the ENSO index (grey bars, right axes). (c, d) Lead–lag cross-correlation of the monthly (c) OH and (d) CO-burden anomaly with the ENSO index (negative lag: ENSO leads).

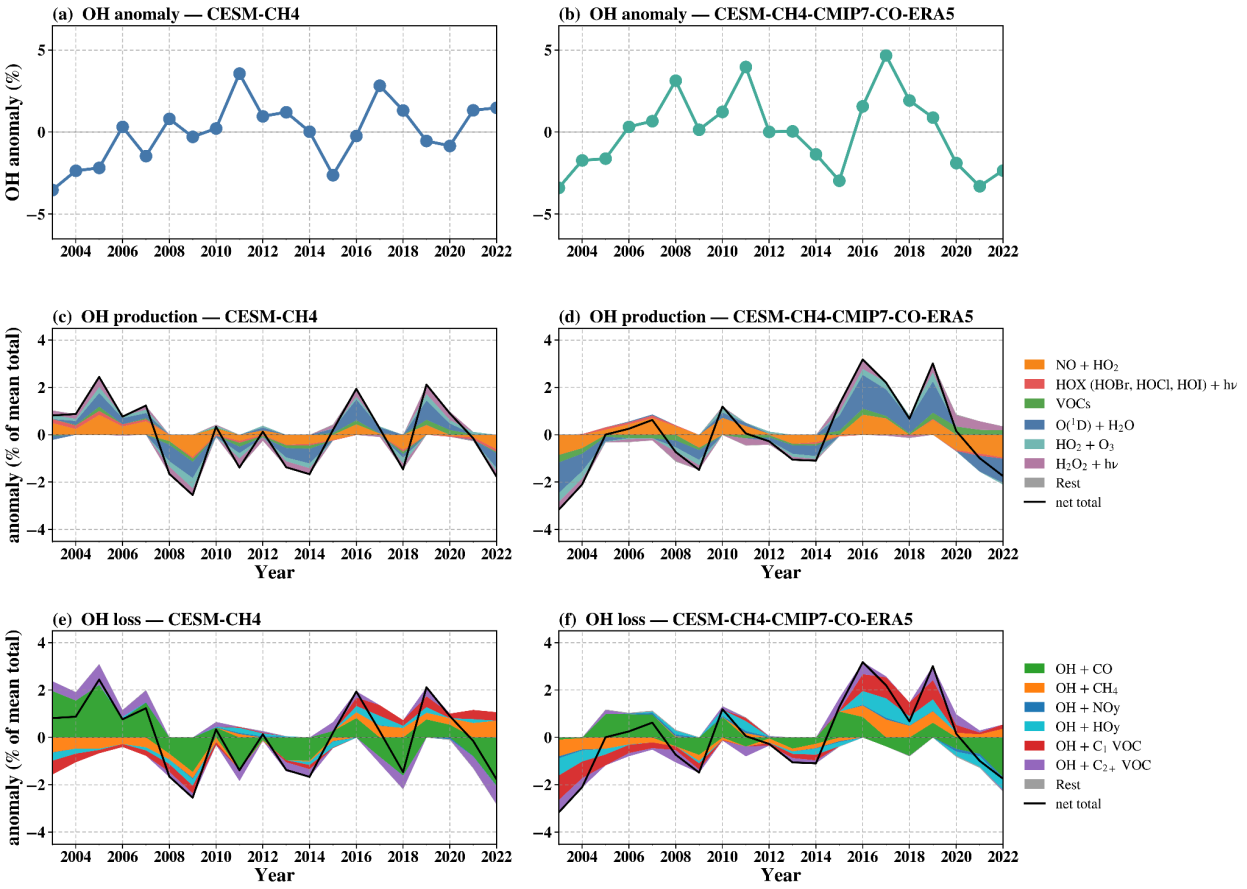



Figure S12. Tropospheric OH budget over 2003–2022 by reaction channel (detrended annual anomalies), for CESM-CH4 (left) and CESM-CH4-CMIP7-CO-ERA5 (right). (a, b) OH anomaly (%); (c, d) production and (e, f) loss channels (%), stacked about zero, with the net as the black line.

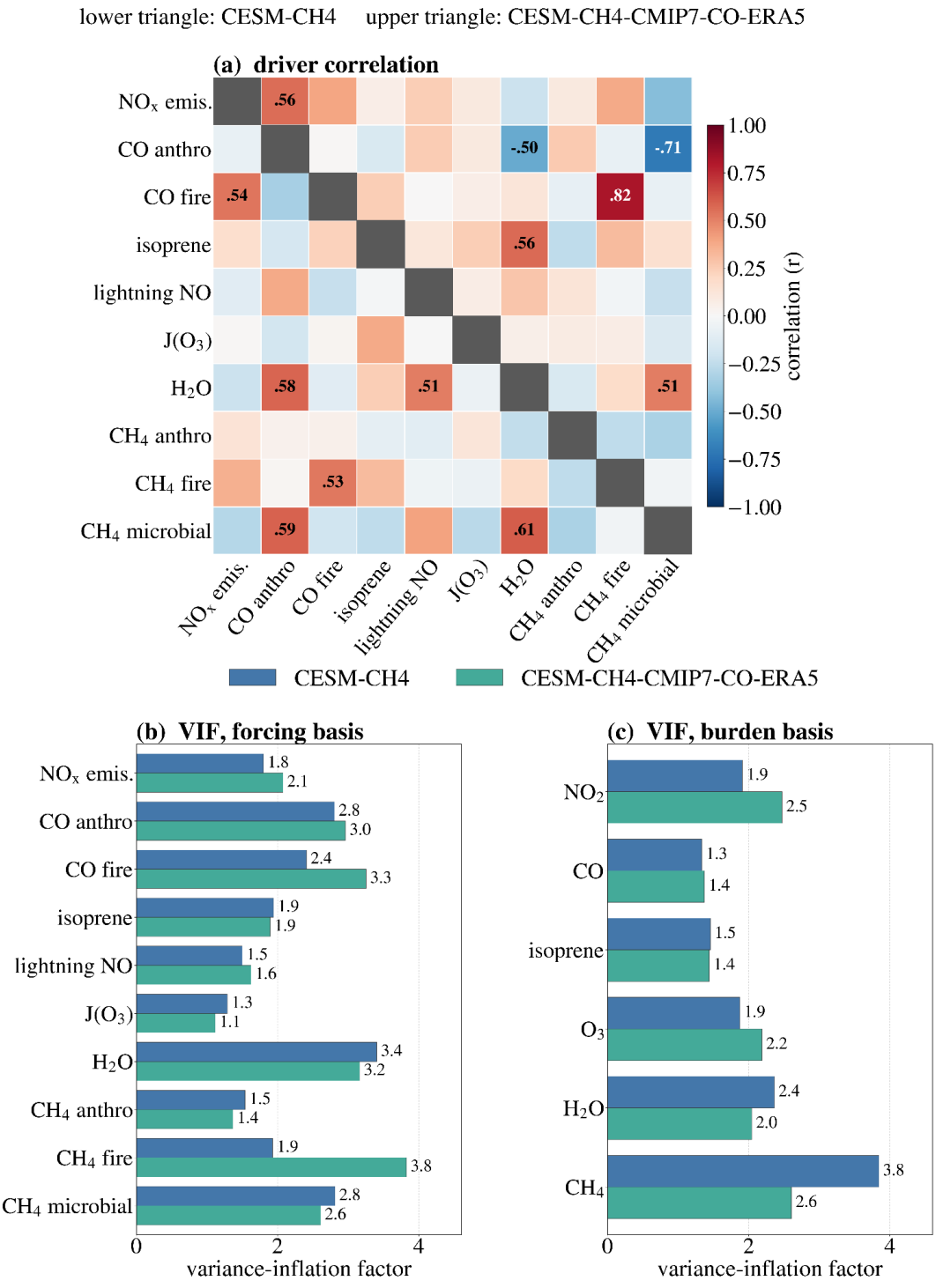



Figure S13. Correlation between forcing-basis predictor anomalies within each regression band, 2003–2022: (a) >30°N , (b) 0–30°N, (c) 0–30°S, (d) >30°S. Lower triangle CESM-CH4, upper triangle CESM-CH4-CMIP7-CO-ERA5.

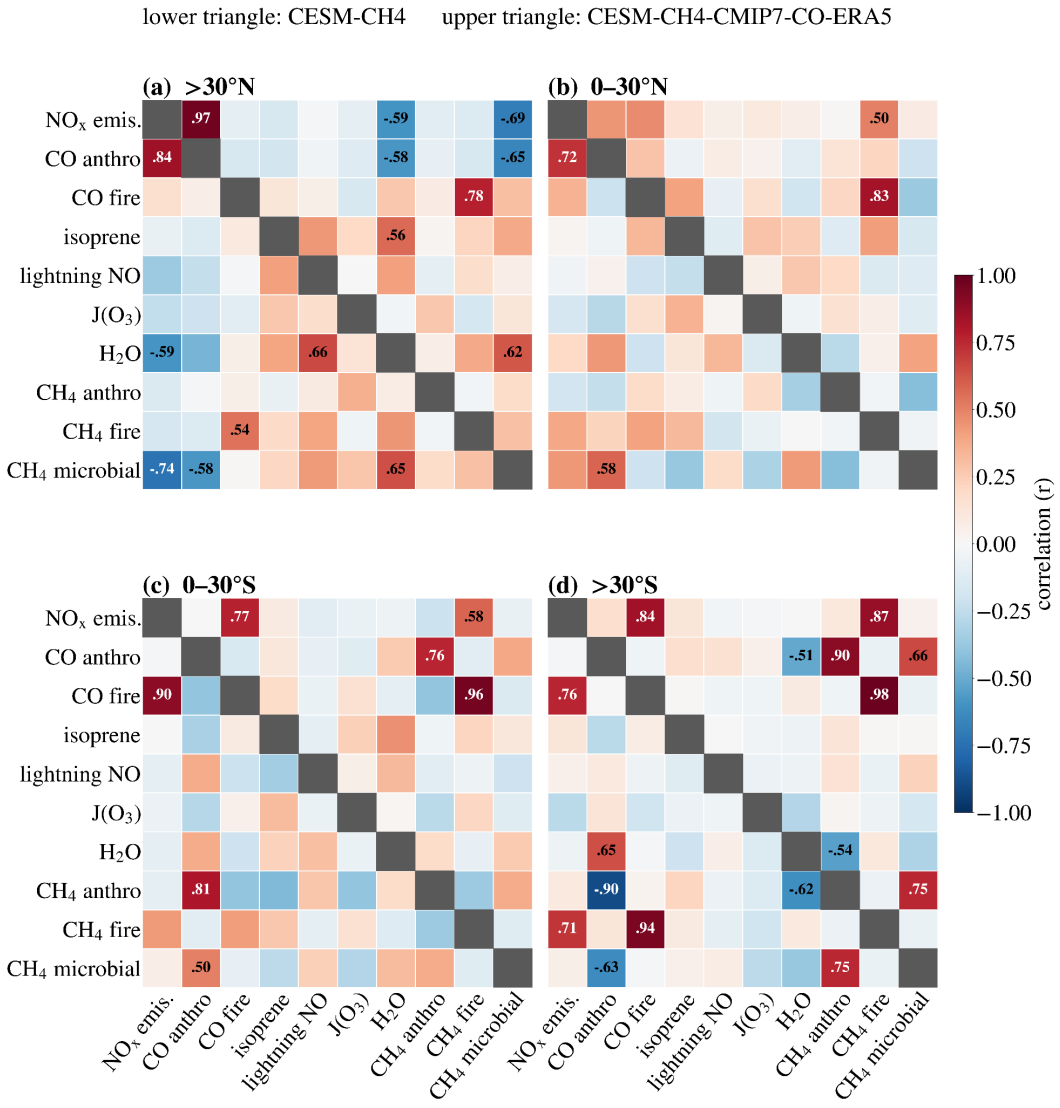



Figure S14.Correlation between forcing-basis predictor anomalies within each regression band, 2003–2022: (a) >30°N , (b) 0–30°N, (c) 0–30°S, (d) >30°S. Lower triangle CESM-CH4, upper triangle CESM-CH4-CMIP7-CO-ERA5.

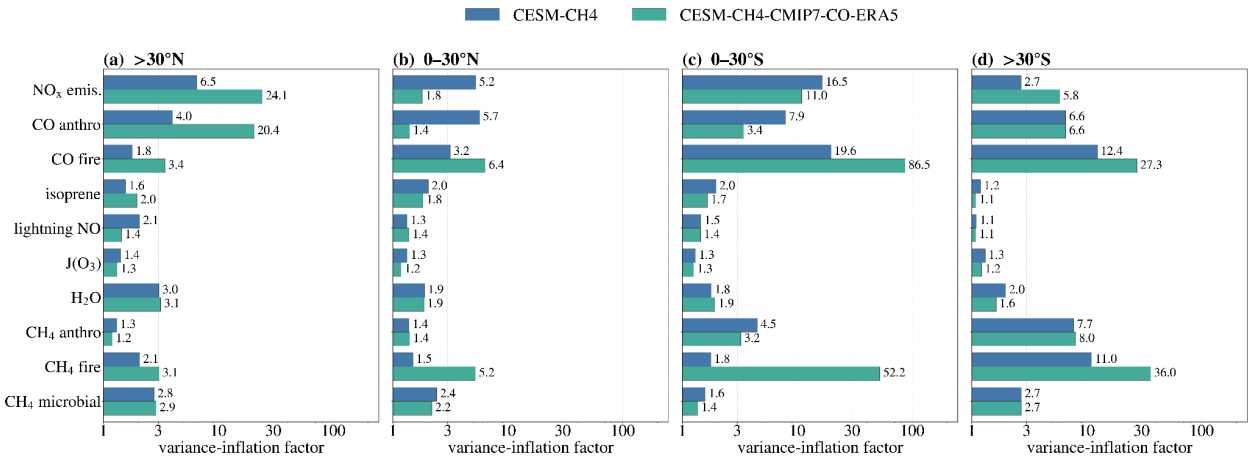



Figure S15. Variance-inflation factor, VIF, of each forcing-basis predictor within each regression band for CESM-CH4 (blue) and CESM-CH4-CMIP7-CO-ERA5 (green): (a) >30°N, (b) 0–30°N, (c) 0–30°S, (d) >30°S.

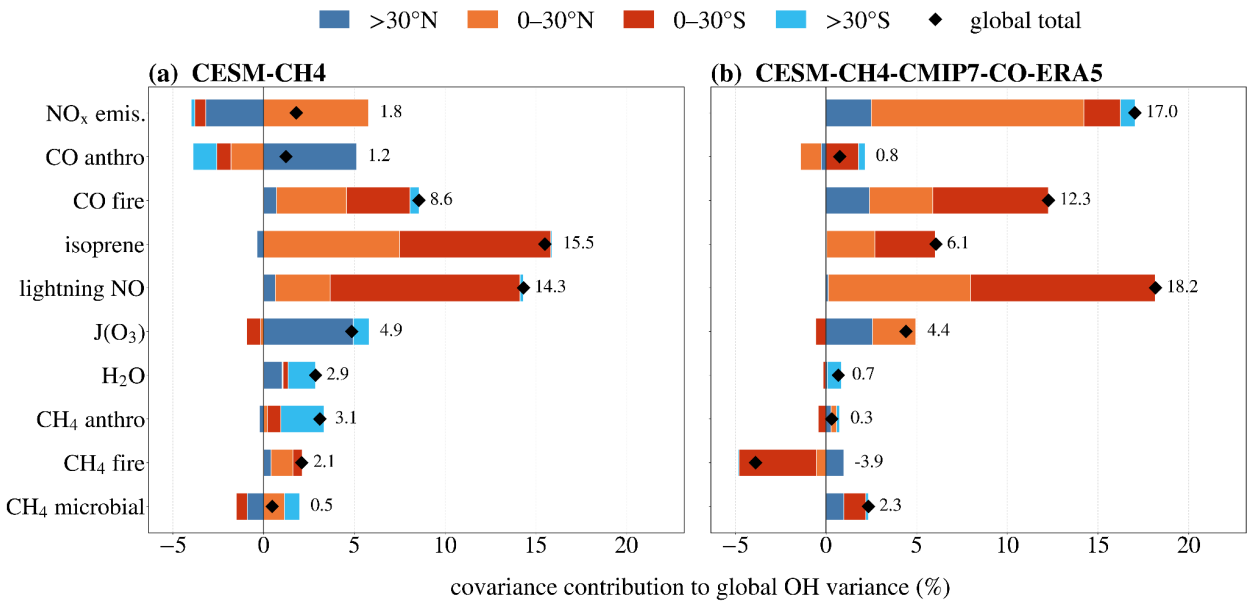



Figure S16. Covariance contribution of each forcing-basis predictor to the variance of the global loss-weighted OH anomaly, split by regression band, for (a) CESM-CH4 and (b) CESM-CH4-CMIP7-CO-ERA5.